Journal of Asian Concrete Federation

journal homepage: https://jacf.sfulib3.publicknowledgeproject.org/index.php/jacf

3D meso-scale finite element analysis of FRP-confined concrete

Jia-Qi Yang [a,b], Yuhang Jin [a], Peng Feng [c], Zeyuan Wang [d,e]

[a] *School of Mechanics and Civil Enginnering, China Unviersity of Mining and Technology (Beijing), Beijing 100083, China;*
[b] *Beijing Key Laboratory of Muti-infrastructure Foundation Modeling and Resilience Enhancement, Beijing 100083, China;*
[c] *Key Laboratory of Civil Engineering Safety and Durability of Ministry of Education, Department of Civil Engineering, Tsinghua University, Beijing 100084, China;*
[d] *National Centre of Technology Innovation for Green and Low-Carbon Building, Beijing 100088, China*
[e] *China Coal Technology and Engineering Group, Beijing 100013, China*

A B S T R A C T

Fibre-reinforced polymer (FRP)-confined concrete demonstrates strain hardening behaviour under compression. This advantageous mechanical behaviour has been extensively utilized in composite structural design and research. To explore the mechanism of the passive confining effect and the internal damage propagation of concrete, a meso-scale finite element (FE) analysis is performed. In this analysis, concrete is regarded as a three-phase heterogeneous material composed of aggregate, cement matrix, and the interfacial transition zone (ITZ). In this paper, existing meso-scale modelling methods and their key parameters are reviewed. Subsequently, a parametric study is conducted, revealing that the parameter values adopted from existing literature are unsuitable for the passively confined scenario. Consequently, a modification to the key parameters is proposed. Using the proposed modelling approach, FRP-confined concrete cylinders and prisms under axial and eccentric compression are modelled. The results unveil the internal damage evolution and the actual stress distribution within FRP-confined concrete, thus providing a deeper understanding of the mechanism of passive confinement.

Keywords: FRP-confined concrete; Meso-scale model; Concrete damage plasticity; ITZ; Non-uniform confinement.

1. Introduction

Fibre-reinforced polymer (FRP) is a composite material characterized by high strength, low weight, and anti-corrosive properties, and it has been extensively studied and applied in the construction industry [1]. An important application of FRP in construction is to confine concrete structural members in compression such as columns and piers. Concrete is a brittle material that is highly sensitive to confinement. With an increase in confining stress, both its compressive strength and ultimate strain are enhanced [2][3][4][5]. If the confining stress is unchanged with the concrete deformation during loading, it is categorized as active confinement. Examples include triaxial tests and concrete confined by steel spirals after the steel yields [6]. Since FRP is a linear elastic material, the confining stress provided by FRP increases linearly with the lateral expansion of concrete during axial compression. This is categorized as passive confinement [7][8]. When there is sufficient FRP confinement, the axial stress-strain curve of concrete exhibits a bilinear ascending until FRP rupture [9][10]. This behaviour is highly beneficial in structural engineering, particularly in resisting seismic actions and progressive collapse. Based on this, various strengthening techniques [11] and composite columns such as CFFT [12][13][14], DSTC [15][16] and FCCC [15][16][17] have been proposed and investigated.

To date, researchers have proposed various analytical models to explain and predict this phenomenon [20]. These models can be categorized into two types: (1) design-oriented models (e.g., [7][21]) and (2) analysis-oriented models (e.g., [8][22][23][24]). The former predefined the equations for the stress-strain curve with undetermined parameters and calibrate them using test data. In contrast, the latter employ an actively confined model in conjunction with an equation depicting the relationship between axial and lateral strains. The stress-strain curve can then be solved iteratively by assuming a compatibility condition between the lateral expansion of

*Corresponding author: Jia-Qi Yang (yangjiaqi@cumtb.edu.cn)

DOI http://dx.doi.org/10.18702/acf.2026.12.1.13

Received: 30-Oct-2025; Revised: 07-Dec-2025; Accepted: 23-Dec-2025; Published online: 31-March-2026

ISSN 2465-7964/eISSN 2465-7972 Copyright © Asian Concrete Federation, All rights reserved.

concrete and the hoop tension of FRP. Yang and Feng [25] proposed a 3D geometric approach that reveals the mechanism of the existing analysis- and design-oriented models. Moreover, this methodology is extended to high-strength concrete [26] and filament-wound FRP tube confinement [27][28]. The series of research indicate that both design-oriented or the analysis-oriented models are phenomenon-based, and thus requires test results for model calibration. The accuracy of these models depends on the database, and the they cannot provide insights to physical changes within the confined concrete. In addition, these models are only applicable to uniformly confined concrete, i.e., FRP-confined concrete cylinders under axial compression. However, the uniformly confined scenario is seldom encountered in engineering practice. In concrete frames, the columns are subjected to combined compression and bending action, and rectangular or square sections are commonly adopted in engineering design. Experimental investigations show that the FRP confinement for columns with rectangular section or under eccentric load can improve ductility, but is less effective in enhancing the compressive strength [29][30][31]. Therefore, investigating the actual stress distribution is a key issue and a prerequisite for developing design methods for engineering application.

In fact, it is challenging to measure the localized stress distribution for concrete under non-uniform confinement. One approach is to directly measure the stress using piezoelectric smart aggregate [32][33][34] or flexible pressure sensors [35][36]. Another solution is to perform macro-scale finite element (FE) analysis. In this kind of models, concrete is regarded as a homogeneous continuum solid, which requires accurate constitutive models for concrete. The constitutive models typically rely on the theory of plasticity, with parameters calibrated using triaxial test data [37][38][39]. Based on macro-scale FE analysis, researchers have proposed analytical models to predict the stress-strain behaviour of non-uniformly confined concrete, such as circular column under eccentric load [40], rectangular and elliptical section column under axial compression [41][42].

Meso-scale finite element modelling offers an effective means of gaining insights into the mechanism and damage evolution of concrete. Unlike traditional constitutive models that assume concrete to be a continuum solid, meso-scale models regard concrete as a multi-phase heterogenous material consisting of aggregates, cement matrix, interfacial transition zones, voids, etc. These models can simulate the random distribution and interaction of different components within the concrete specimen. This modelling approach is extensively employed in the analysis of concrete damage and fracturing under compression, tension, and shear. Therefore, it is a viable solution for investigating the physical mechanism and stress distribution of FRP-confined concrete. Although the meso-scale modelling approaches have become increasingly mature to date, several research gaps remain to be addressed. Firstly, some constitutive laws at the meso-scale level are challenging to test directly, and the trial-and-error method is often used as a makeshift. Most researchers calibrate the model parameters based on their own tests. Thus, their recommended parameter values may not be applicable in generalized scenarios. Therefore, it is essential to explore the influence of key parameters and provide justifications for the parameter values. Secondly, most existing models concentrate on uniaxial compression, flexural tension, and splitting cracking, while only a limited number of studies consider the biaxial compression state. These are mainly 1D or 2D stress states. FRP-confined concrete is subjected to triaxial compression, yet there is a lack of research in this area.

This paper aims to reveal the physical mechanism and actual stress distribution of FRP-confined concrete through meso-scale finite element analysis. Initially, recent modelling techniques and values of key parameters are reviewed. Subsequently, a parametric study is carried out to examine the influence of each parameter. As a result, a set of key parameter values is recommended. Finally, using the proposed parameters, FRP-confined concrete cylinders and prisms under axial and eccentric compression are modelled. The macro-scale behaviour of the models are in good agreement with the test curves, and the damage patterns and internal stress distribution confirm the recent experimental findings. In states like Rajasthan, accumulated deposits already exceed 100 million tons [8]. Addressing both challenges together opens opportunities for circular economic solutions. Recycling dimensional stone waste into new construction materials reduces the demand for virgin resources and diverts large volumes of waste from disposal sites. Geopolymer technology offers one such route. Geopolymers are inorganic binders formed through the reaction of aluminosilicate precursors with alkaline activators [9]. Compared with ordinary Portland cement (OPC), geopolymers can lower greenhouse gas emissions by up to 80% and can incorporate a wide range of industrial by-products, including fly ash, slag, and stone dust [10,11].

2. Review of existing modelling approaches

This section provides a review of recent publications on the meso-scale modelling of concrete spanning from 2015 to 2024. The modelling techniques and values of key parameters are summarized in Table A1 and will be discussed as follows.

2.1 Meso-scale modelling strategies

At the meso-scale level, the characteristics of concrete are as follows: Firstly, it consists of multiple phases, including aggregate, mortar matrix, and interfacial transition zone. Secondly, the size, shape, and distribution of the aggregates exhibit randomness. Finally, each phase has its own mechanical behaviour. By reviewing the recent publications, the modelling strategies can be summarized from the following five aspects:

(1) FE Mesh. Two approaches are available for discretizing the geometries of different components into finite elements: (i) direct meshing ([50]-[68]) and (ii) grid mapping meshing ([43][44][45][46][47][48][49]). For the direct meshing approach, the geometries of concrete components are first modelled.

Subsequently, these geometries are meshed into finite elements and assigned corresponding material properties. Given the complex shape of aggregates, 4-node tetrahedral elements are typically used in 3D analysis, and 3-node triangular elements are employed in 2D analysis. This method can effectively represent the geometry of aggregates. Nevertheless, due to this complexity, the elements may exhibit irregular or distorted shapes, which pose challenges to convergence. For the grid mapping meshing approach, the domain of the specimen is meshed into uniform and fine grids. In 3D models, these are usually 8-node hexahedral elements, and in 2D models, 4-node quadrilateral elements. Subsequently, different regions within the domain are identified as aggregates, mortar matrix, and ITZ and are assigned corresponding properties. This method has good convergence, but its accuracy depends on the grid size. A large number of elements may consume substantial computing power.

(2) Number of phases. As previously mentioned, concrete consists of aggregate, mortar matrix, and the interfacial transition zone (ITZ). Depending on the problems under focus, the meso-scale model can be two-, three-, or even four-phased. For two-phase models, only the aggregate and mortar matrix are modelled. The ITZ is disregarded, and the aggregate and mortar matrix are assumed to be perfectly bonded [43][50]. Three-phase models consider the aggregates, mortar matrix, and ITZ separately, which is the most commonly used approach in the reviewed literature. Additionally, some studies concentrate on the influence of defects in concrete. In such cases, the voids become the fourth phase and are assigned a null or very low modulus [63].

(3) Constitutive Model of the ITZ. There are two approaches for modelling the ITZ. Firstly, the ITZ is modelled as a continuum solid with a finite thickness. The material models of this type of model are a reduction of those of the mortar matrix [51][52][53][54][55]. This method is frequently used in conjunction with the grid mapping mesh method [43][44][46][47][48][49]. Secondly, the ITZ is modelled using cohesive elements assigned with traction-separation laws. The thickness of the cohesive elements can be either finite or zero, and the traction-separation law encompasses stress-displacement behaviours in both the normal and transverse directions [56][57][58][59][60][61][62][63][64][65][66][67][68]. The cohesive elements take into account the stiffness (kN and kS), bond strength (fN and fS), and fracture energy (GN and GS) of the aggregate-to-mortar interface, where N and S represent the normal and shear directions, respectively.

(4) Constitutive model of the mortar matrix. Two methods are available for modelling the mortar matrix. The first approach considers the mortar as a continuum solid with a constitutive relationship based on plasticity. Typical examples include the concrete damage plasticity (CDP) model [69], elastic-viscoplastic damage (EVPD) model [51], K&C model [57], etc. The second method assigns linear elastic behaviour to the mortar elements and inserts cohesive elements between adjacent mortar elements, herein denoted as the M-M interface [45][56][60][61][62][63][64][65][66][67][68]. This is similar to the discrete element method (DEM), which only takes into account the interactions of particles.

(5) Constitutive model of aggregates. Given that the strength of aggregates is significantly higher than that of mortar and the ITZ, most existing literatures treat the aggregates as linear elastic materials. Additionally, some studies explore the damage of aggregates (such as in lightweight aggregate concrete [67]). Thus, aggregates are still modelled as linear elastic, but cohesive elements are inserted between adjacent aggregate elements, herein denoted as the A-A interface [45][56][62][66][67][68].

This study focuses on the behaviour of FRP-confined concrete cylinders and prisms. Taking both accuracy and computational efficiency into account, the modelling strategy adopted for this research is as follows: (1) directly mesh on geometries; (2) Consider three phases, namely aggregate, mortar matrix, and ITZ; (3) Model the ITZ using zero-thickness cohesive elements with traction-separation laws; (4) Employ the CDP model to simulate the mortar matrix; and (5) Assume the aggregates being isotropic linear elastic.

2.2 Key parameters

The key parameters of the reviewed papers are presented in Table 1. In accordance with the modelling strategy described in section 2.1, the key parameters taken into account in the current model are as follows.

(1) Aggregate: Elastic modulus (Ea) and Poisson's ratio (νa).

(2) Mortar: Elastic modulus (Em) and Poisson's ratio (νm), compressive strength (fc), tensile strength (ft), friction angle (β) and dilation angle (ψ). In the CDP model, the friction angle is indirectly defined by the ratio of biaxial compressive strength and uniaxial compressive strength (fb/fc). The yield surface of the CDP model in the tri-axial compression state is:

$$F = \frac{1}{1-\alpha}(\bar{q} - 3\alpha\bar{p} - \gamma\langle -\bar{\sigma}_{max}\rangle) - \bar{\sigma}_c\left(\varepsilon_c^{pl}\right) = 0 \quad (1)$$

where p is the effective hydraulic pressure (positive in compression), q is the effective Mises equivalent stress, σmax is the effective maximum principal stress (positive in tension), and σcεcpl is the effective compressive cohesion stress. In EQ.1, the α is:

$$\alpha = \frac{(f_{b0}/f_{c0}) - 1}{2(f_{b0}/f_{c0}) - 1} \quad (2)$$

Therefore, as shown in Fig. 1, the friction angle yields:

$$\tan(\beta) = 3\alpha = \frac{3(f_b/f_c) - 3}{2(f_b/f_c) - 1} \quad (3)$$

The ABAQUS recommended value for fb/fc is 1.16, therefore the default friction angle $\beta = 20^\circ$.

(3) ITZ: The cohesive elements of the ITZ adhere to the traction-separation law, which is expressed in terms of stress-displacement in both the normal and shear directions. As depicted in Fig. 2, the stress-displacement relationships are linear in the elastic stage, with the stiffness denoted as kN and kS in the normal and shear directions, respectively. The

quadratic criterion is employed for damage initiation:

$$\begin{cases}\sigma_N = k_N\delta_N \\ \tau = k_S\delta_S\end{cases} \tag{4}$$

$$\left[\frac{\langle\sigma_N\rangle}{f_N}\right]^2 + \left[\frac{\tau}{f_s}\right]^2 = 1 \tag{5}$$

where kN and kS are the normal and shear stiffness, and δN and δS are the normal and shear displacement, respectively. σN and τ are tensile and shear stress, respectively. The "< · >" is the Macaulay bracket. fN and fS denote the tensile and shear strength for the interface. When damaged, the stress-displacement relationship becomes:

$$\begin{cases}\sigma_N = (1-D)k_N\delta_N \\ \tau = (1-D)k_S\delta_S\end{cases} \tag{6}$$

where $0 \leqslant D \leqslant 1$ is the damage variable which determines the post-peak shape of the stress-displacement curve. Hence, the fracture energy can be calculated as:

$$\begin{cases}G_N = \int_0^{\delta_{N,f}} \sigma_N d\delta_N \\ G_S = \int_0^{\delta_{S,f}} \tau d\delta_S\end{cases} \tag{7}$$

where the subscript f denotes the displacement at failure when D=1, and GN and GS are Mode I and Mode II fracture energy, respectively. When the cohesive element is under combined normal and shear actions, the Benzeggagh-Kenane (BK) criteria [70] is applied. According to preliminary parametric study, the mix-mode factor η has limited influence on the results, therefore it is chosen to be 1.2 following the suggestion of [62].

The above-mentioned key parameters are extracted from Table 1 for reference in the current model. The ranges and average values are presented in Table 2. It should be noted that only a portion of the collected papers fully aligns with the current modelling strategy. Consequently, the number of effectively reported values for each parameter varies, as shown in the table.

The CDP model requires uniaxial compression and tension stress-strain curves of concrete. Here, the curves provided by the Chinese code GB50010-2010 [71] are employed for the mortar. For the uniaxial compression, the equations for the stress-strain curve are:

$$\sigma_c = (1-d_c)E_m\varepsilon_c \tag{8}$$

$$d_c = \begin{cases}1 - \dfrac{\rho_c n}{n - 1 + (\varepsilon_c/\varepsilon_{c,r})^n} & \varepsilon_c/\varepsilon_{c,r} \leq 1 \\ 1 - \dfrac{\rho_c}{\alpha_c(\varepsilon_c/\varepsilon_{c,r} - 1)^2 + \varepsilon_c/\varepsilon_{c,r}} & \varepsilon_c/\varepsilon_{c,r} > 1\end{cases} \tag{9}$$

$$\rho_c = \frac{f_c}{E_m\varepsilon_{c,r}} \tag{10}$$

$$n = \frac{E_m\varepsilon_{c,r}}{E_m\varepsilon_{c,r} - f_c} \tag{11}$$

$$\alpha_c = 0.157f_c^{0.785} - 0.905 \tag{12}$$

where fc is the compressive strength of the mortar matrix (in MPa), and εc,r is the corresponding compressive strain. αc is a unitless factor. Em is the elastic modulus of the mortar matrix (in MPa). The relationship between fc and εc,r is:

$$\varepsilon_{c,r} = (700 + 172\sqrt{f_c}) \times 10^{-6} \tag{13}$$

For uniaxial tension, the stress-strain behaviour is:

$$\sigma_t = (1-d_t)E_m\varepsilon_t \tag{14}$$

$$d_t = \begin{cases}1 - \rho_t(1.2 - 0.2(\varepsilon_t/\varepsilon_{t,r})^5) & \varepsilon_t/\varepsilon_{t,r} \leq 1 \\ 1 - \dfrac{\rho_t}{\alpha_t(\varepsilon_t/\varepsilon_{t,r} - 1)^{1.7} + \varepsilon_t/\varepsilon_{t,r}} & \varepsilon_t/\varepsilon_{t,r} > 1\end{cases} \tag{15}$$

$$\rho_t = \frac{f_t}{E_m\varepsilon_{t,r}} \tag{16}$$

$$\alpha_t = 0.312f_t^2 \tag{17}$$

where ft is the tensile strength of the mortar matrix (MPa), and εt,r is the corresponding tensile strain. αt is a unitless factor. The relationship between ft and εt,r is:

$$\varepsilon_{t,r} = f_t^{0.54} \times 65 \times 10^{-6} \tag{18}$$

With EQs. 8-18, the uniaxial stress-strain curves for compression and tension can be determined with known fc, ft and Em. If ft is not available, it can be calculated with [71]:

$$f_t = 0.404f_c^{0.55} \tag{19}$$

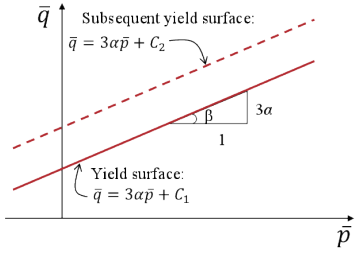

Figure 1. Friction angle

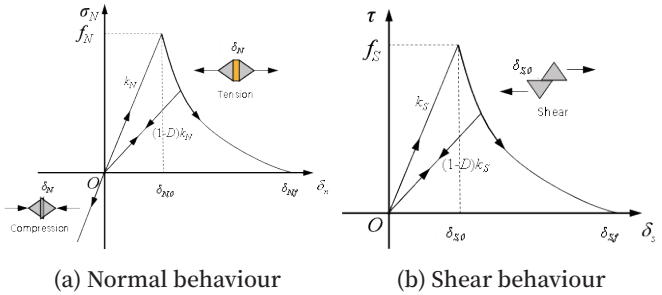

(a) Normal behaviour (b) Shear behaviour

Figure 2. Traction-separation law

Table 1. Meso-scale modelling strategies and key parameters in literature (1/4)

Ref.	Meshing strategy	Component	Constitutive model	Key parameters
[43]	2D Mapping mesh	Aggregate	Elastic	Ea=70GPa, νa=0.2
		Mapping mesh	CDP	Em=25GPa, νm=0.2, ft=4MPa, fc=45MPa, β=20° , ψ=30°
[44]	3D Mapping mesh	Aggregate	Elastic	Ea=50GPa
		Mapping mesh	CDP	Em=20GPa, fc=35MPa, ft=4.5MPa, β=20° , ψ=31°
		ITZ	CDP	EITZ=15GPa, fc=27MPa, ft=3.5MPa, β=20° , ψ=31°
[45]	3D Mapping mesh	Aggregate	Elastic	Ea=45.5GPa, νa=0.2
		Mapping mesh	Elastic	Em=30GPa, νm=0.23
		ITZ	Cohesive	fN=2.1MPa, GN=0.0062N/mm, fS=4.1MPa, GS=0.062N/mm
		M-M interface	Cohesive	fN =3MPa, GN =0.08N/mm, fS =10.5MPa, GS=0.8N/mm
		A-A interface	Cohesive	fN =15MPa, GN =0.161N/mm, fS =20MPa, GS=1.61N/mm
[46]	3D Mapping mesh	Aggregate	Elastic	Ea=50GPa
		Mapping mesh	CDP	Em=30.9GPa, fc=35.6MPa, ft=3.05MPa, β=20° , ψ=38°
		ITZ	CDP	EITZ=10.3GPa, fc=4.2MPa, ft=0.28MPa, β=20° , ψ=38°
[47]	3D Mapping mesh	Aggregate	CDP	Ea=70.1GPa, νa=0.2, G=0.06N/mm
		Mapping mesh	CDP	Em=30.8GPa, νm=0.2, fc=45.3MPa, ft=3.8MPa, β=20° , ψ=18°
		ITZ	CDP	EITZ=24.7GPa, νITZ=0.2, fc=37.2MPa, ft=3.3MPa, β=20° , ψ=15°
[48]	3D Mapping mesh	Aggregate	CDP	Ea=50GPa, νa=0.16, fc=130MPa, ft=10MPa, β=20° , ψ=30°
		Mapping mesh	CDP	Em=30GPa, νm=0.2, fc=30MPa, ft=3MPa, β=20° , ψ=30°
		ITZ	CDP	EITZ=26GPa, νITZ=0.22, fc=28.4MPa, ft=2.8MPa, β=20° , ψ=30°
[49]	3D Mapping mesh	Aggregate	CDP	Ea=60GPa, νa=0.16, fc=80MPa, ft=8MPa, β=20° , ψ=30°
		Mapping mesh	CDP	Em=32.5GPa, νm=0.2, fc=40MPa, ft=4MPa, β=20° , ψ=18°
		ITZ	CDP	EITZ=26GPa, νITZ=0.22, fc=32MPa, ft=3.2MPa, β=20° , ψ=15°
[50]	2D Direct mesh	Aggregate	Elastic	Ea=50GPa, νa=0.16
		Direct mesh	CDP	Em=22.4GPa, νm=0.2, ft=3.57MPa, fc=37.46MPa, β=20° , ψ=30°
		ITZ	/	Perfectly bond
[51]	3D Direct mesh	Aggregate	Elastic	Ea=40GPa, νa=0.2
		Direct mesh	EVPD	Em=20GPa, νm=0.2, c=10MPa, φ=50° , ft=3.5MPa
		ITZ	EVPD	EITZ=12GPa, νITZ=0.2, c=6MPa, φ=36° , ft=2.1MPa

Table 1. (continued 2/4)

Ref.	Meshing strategy	Component	Constitutive model	Key parameters
[52]	2D Direct mesh	Aggregate	Elastic	Ea=80GPa, νa=0.16,
		Direct mesh	CDP	Em=25GPa, νm=0.22, fc=45MPa, ft=3MPa, β=20° , ψ=30-31°
		ITZ	CDP	EITZ=20GPa, νITZ=0.2, fc=35MPa, ft=2.4MPa, β=20° , ψ=30-31°
[53]	2D Direct mesh	Aggregate	Elastic	Ea=80GPa, νa=0.16,
		Direct mesh	CDP	Em=26GPa, νm=0.22, fc=45MPa, ft=3MPa, β=20° , ψ=30°
		ITZ	CDP	EITZ=20GPa, νITZ=0.2, fc=30MPa, ft=2.4MPa, β=20° , ψ=30°
[54]	2D Direct mesh	Aggregate	Elastic	Ea=43GPa, νa=0.23
		Direct mesh	CDP	Em=25GPa, νm=0.2, fc=35MPa, ft=3.5MPa, β=20°
		ITZ	CDP	EITZ=18GPa, νITZ=0.2, fc=20MPa, ft=3MPa, β=20°
[55]	2D Direct mesh	Aggregate	Elastic	Ea=70GPa, νa=0.2
		Direct mesh	CDP	Em=25GPa, νm=0.2, fc=45MPa, ft=4MPa, β=20° , ψ=35°
		ITZ	CDP	EITZ=22GPa, νITZ=0.2, fc=22.5MPa, ft==2MPa, β=20° , ψ=35°
[57]	2D Direct mesh	Aggregate	Elastic	Ea=60GPa, νa=0.2
		Mortar	K&C	Em=30GPa, νm=0.2, fc=45MPa
		ITZ	Cohesive	kN=kS=1.5×10^{6}MPa/mm, fN =2.3MPa, GN=0.03N/mm, fS =9.2MPa, GS =0.3N/mm
[58]	3D Direct mesh	Aggregate	Elastic	Ea=45GPa, νa=0.2
		Mortar	CDP	Em=20.2GPa, νm=0.2, fc=56.5MPa, ft=3.7MPa, β=20° , ψ=20-35°
		ITZ	Cohesive	kN=kS=1×10^{5}MPa/mm, fN=3.5MPa, GN=0.03-0.05N/mm, fS=10.5MPa, GS=0.09N/mm
[59]	3D Direct mesh	Aggregate	Elastic	Ea=70GPa, νa=0.2
		Mortar	CDP	Em=25GPa, νm=0.2, fc=45MPa, ft=4MPa, β=20° , ψ=35°
		ITZ	Cohesive	kN=kS=1×10^{6}MPa/mm, fN=2.6MPa, GN=0.025N/mm, fS=10MPa, GS=0.0625N/mm
[60]	3D Direct mesh	Aggregate	Elastic	Ea=70GPa, νa=0.2
		Mortar	Elastic	Em=25GPa, νm=0.2
		ITZ	Cohesive	kN=kS=1×10^{6}GPa/mm, fN =1.5MPa, GN =0.02N/mm, fS=5.25MPa, GS=0.2N/mm
		M-M interface	Cohesive	kN=kS=1×10^{6}GPa/mm, fN =3MPa, GN =0.04N/mm, fS=10.5MPa, GS =0.4N/mm

Table 1. (continued 3/4)

Ref.	Meshing strategy	Component	Constitutive model	Key parameters
[61]	3D Direct mesh	Aggregate	Elastic	Ea=70GPa, νa=0.2
		Mortar	Elastic	Em25GPa, νm0.2
		ITZ	Cohesive	kN=kS=1×10^{6}MPa/mm, fN =3MPa, GN=0.02N/mm, fS=10.5MPa, GS=0.2N/mm
		M-M interface	Cohesive	kN=kS=1×10^{6}MPa/mm, fN =4MPa, GN=0.04N/mm, fS=30MPa, GS=0.4N/mm
[62]	2D Direct mesh	Aggregate	Elastic	Ea=72GPa, νa=0.16
		Mortar	Elastic	Em=8GPa, νm0.2
		ITZ	Cohesive	kN=kS=1×10^{4}MPa/mm, fN=2.6MPa, GN=0.025N/mm, fS=10MPa, GS=0.625N/mm
		A-A interface	Cohesive	fN=6-15MPa, GN=60-1400N/mm, fS=40-120MPa, GS=1500-35000N/mm
		M-M interface	Cohesive	kN=kS=1.8×10^{4}MPa/mm, fN=4MPa, GN=0.1N/mm, fS=30MPa, GS=2.5N/mm
[63]	3D Direct mesh	Aggregate	Elastic	Ea=70GPa, νa=0.2
		Mortar	Elastic	Em=25GPa, νm=0.2
		ITZ	Cohesive	kN =1.82×10^{5}MPa/mm, fN=0.4MPa, GN=0.01N/mm
		M-M interface	Cohesive	kN =1.82×10^{5}MPa/mm, fN=1MPa, GN=0.02N/mm
[64]	3D Direct mesh	Aggregate	Elastic	Ea=70GPa, νa=0.2
		Mortar	Elastic	Em=25GPa, νm=0.22
		ITZ	Cohesive	kN=1.92×10^{5}MPa/mm, fN=0.4MPa, GN=0.015N/mm
		M-M interface	Cohesive	kN=1.92×10^{5}MPa/mm, fN=1MPa, GN=0.03N/mm
[65]	2D Direct mesh	Aggregate	Elastic	Ea=50GPa
		Mortar	Elastic	Em=20GPa
		ITZ	Cohesive	kN=kS=5×10^{5}MPa/mm, fN=5MPa, GN=0.1N/m, fS=10MPa, GS=2.5N/mm
		M-M interface	Cohesive	kN=kS=5×10^{5}MPa/mm, fN=1.25MPa, GN=0.025N/mm, fS=2.5MPa, GS=0.625N/mm

Table 1. (continued 4/4)

Ref.	Meshing strategy	Component	Constitutive model	Key parameters
[66]	2D Direct mesh	Aggregate	Elastic	Ea=75GPa, νa=0.16
		Mortar	Elastic	Em=35GPa, νm=0.2
		ITZ	Cohesive	kN=kS=1×10^{6}MPa/mm, fN=3MPa, GN=0.04N/mm, fS=12MPa, GS=0.12N/mm
		M-M interface	Cohesive	kN=kS=1×10^{6}MPa/mm, fN=5MPa, GN=0.2N/mm, fS=35MPa, GS=4N/mm
		A-A interface	Cohesive	kN=kS=1×10^{6}MPa/mm, fN==5MPa, GN=400N/mm, fS=35MPa, GS=10000N/mm
[67]	2D Direct mesh	Aggregate	Elastic	Ea=16GPa, νa=0.22
		Mortar	Elastic	Em=38GPa, νm=0.2
		ITZ	Cohesive	kN=kS=1×10^{5}MPa/mm, fN=1.6MPa, GN=0.03N/mm, fS=5MPa, GS=0.3N/mm
		M-M interface	Cohesive	kN=kS=1×10^{5}MPa/mm, fN=2.5MPa, GN=0.05N/mm, fS=15MPa, GS=0.5N/mm
		A-A interface	Cohesive	kN=kS=1×10^{5}MPa/mm, fN=5.1MPa, GN=0.02N/mm, fS=12MPa, GS=0.2N/mm
[68]	2D Direct mesh	Aggregate	Elastic	Ea=47.2GPa, νa=0.2
		Mortar	Elastic	Em=29.2GPa, νm=0.2
		ITZ	Cohesive	kN=kS=1×10^{6}MPa/mm, fN=1.6MPa, fS=1.6-2.4MPa, G=0.02N/mm
		M-M interface	Cohesive	kN=kS=1×10^{6}MPa/mm, fN=4.4MPa, fS=4.4-6.6MPa, G=0.04N/mm
		A-A interface	Cohesive	kN=kS=1×10^{6}MPa/mm

3. Proposed model

3.1 Details of the meso-scale model

The aggregates are generated using the take-and-place method, which is briefly introduced herein: (1) A reference point Oi=(xi, yi, zi) is generated as a random vector within the domain of the concrete specimen. (2) The radius of the aggregate (ri) is generated in the size interval (m, n) following a uniform distribution. (3) Check the distance between the current aggregate and each of the previously generated aggregate (dij, j=1, 2, ⋯, i-1) as well as its distance to the boundary (diB) (as shown in Fig. 3a). If dij<ri+rj or diB<ri, delete this aggregate and return to step 1. (4) As shown in Fig. 3b, determine the coordinate of the vertices vi=(xik, yik, zik) where k=1, 2, ⋯, 18 using the following equation:

$$\begin{cases} x_{ik} = x_i + r_i \cos(\theta)\cos(\varphi) \\ y_{ik} = y_i + r_i \cos(\theta)\sin(\varphi) \\ z_{ik} = z_i + r_i \sin(\varphi) \end{cases} \tag{20}$$

where θ and ϕ follow uniform distribution in [0, 2π). Consequently, a 18-vertices polyhedron aggregate is generated. (5) Mesh the aggregate using 4-node tetrahedron element, as depicted in Fig. 3c. (6) Repeat steps 1-5 until no more aggregate of the current size interval can be placed. Then, switch to the next interval with a smaller aggregate size. The intervals are selected as [25, 30], [20, 25), [15, 20), [10, 15), and [7.5,10). The total volumetric ratio of the aggregates can reach up to 35%, which is shown in Fig. 3d.

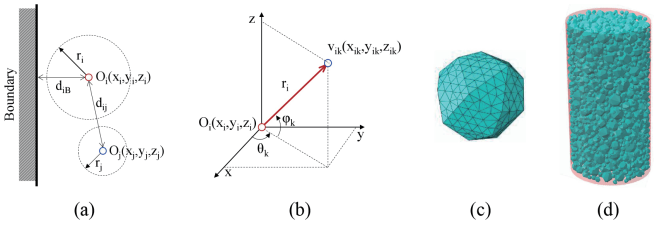

Figure 3. Generation of random aggregate

After generating the aggregates, the mortar matrix is modelled through the Boolean operation and meshed using 4-node tetrahedra elements (C3D4). When meshing the mortar matrix, the node locations on the mortar-aggregate interface are maintained in correspondence with those on the aggregate. This allows for the insertion of zero-thickness cohesive elements with 6 nodes (COH3D6) at the interface, as schematically depicted in Fig. 4. For the FRP-confined concrete specimens, the FRP jacket is meshed using 4-node quadrilateral shell elements with reduced integration (S4R) and is tied to the

surface of the concrete cylinder. The elastic modulus of GFRP and CFRP in the hoop direction are 81300 MPa and 250000 MPa, respectively, which are obtained from flat coupon tensile tests. The nominal thicknesses of a single ply of GFRP and CFRP sheets are 0.170 mm/ply and 0.111 mm/ply, respectively. In the model, the elastic modulus in the axial direction, Poisson's ratio, and shear modulus of the FRP are deliberately set to zero to eliminate the biaxial effect of the confining material [27][28].

Table 2. Ranges of the key parameters

Component	Parameter	Unit	Min	Max	Mean	Counts	Benchmark
Aggregate	Ea	GPa	16.0	80.0	59.4	26	55
	νa	/	0.16	0.23	0.19	23	0.2
Mortar	Em	GPa	20	38	26.7	25	20.2
	νm	/	0.20	0.23	0.20	22	0.2
	fc	MPa	30.0	56.5	41.8	14	56.5
	ft	MPa	3.0	4.5	3.6	14	3.7
	β	°	20	20	20	13	20
	ψ	°	18	38	29.4	12	25
ITZ	kN	MPa/mm	1×10^4	1×10^6	6.6×10^5	13	2.5×10^4
	fN	MPa	0.4	5.0	2.3	14	3
	GN	N/mm	0.0062	0.0400	0.0308	14	0.03
	kS	MPa/mm	1×10^4	1×10^6	7.5×10^5	11	2.5×10^4
	fS	MPa	2.0	15.0	8.3	12	10
	GS	N/mm	0.0200	2.5000	0.3925	12	0.75

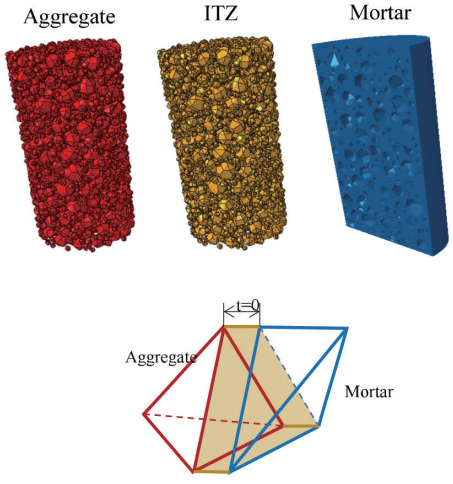

Figure 4. Modelling of ITZ

3.2 Mesh sensitivity

To initiate the simulation, the key parameters presented in Table 2 are utilized as a benchmark. The benchmark parameters are taken from [58]. Unconfined, 1-ply GFRP, and 4-ply CFRP confined concrete cylinders with a diameter of 150 mm and a height of 300 mm are modelled. These cylinders represent unconfined, weakly confined, and moderately confined scenarios, respectively. The cylinders are subjected to axial compression and solved using the dynamic explicit solver in ABAQUS [72]. To ensure the accuracy of the dynamic approach, the ratio between the kinetic energy and the internal energy (ALLKE/ALLIE) is obtained from the result file and plotted in Fig. 5a. Except for the beginning of the loading stage, the ratio approaches to zero, indicating that the success of the dynamic solver in solving quasi-static problem. The element size is refined successively from 6 mm to 5 mm, 3 mm, and finally to 2.5 mm. The axial stress-strain curves for the three models are plotted in Fig. 5b-d. As depicted in the figure, the curves conform to the general characteristics of unconfined and FRP-confined concrete, demonstrating second-portion ascending behaviour. The curves converge when the element size is 3 mm and 2.5 mm. Therefore, the element size is selected as 2.5 mm, which is less than 1/3 of the smallest aggregate. In this case, the total numbers of nodes and elements are 7.37×10^5 and 3.63×10^6, respectively.

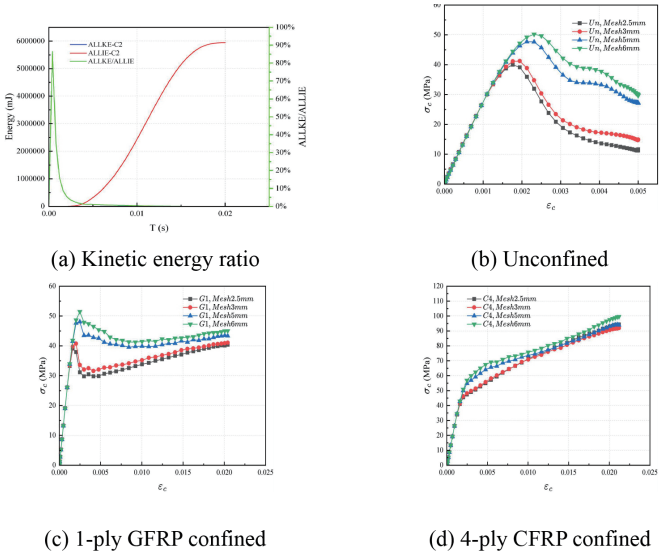

(a) Kinetic energy ratio (b) Unconfined

(c) 1-ply GFRP confined (d) 4-ply CFRP confined

Figure 5. Kinetic energy ratio and mesh sensitivity

3.3 Parametric study

3.3.1 Unconfined concrete

The initial step of the parametric study involves examining the impact of key parameters on the uniaxial compressive behaviour of the unconfined concrete cylinder. Each parameter is altered twice, with the benchmark value set as the median. The results are presented in Fig. 6. As can be seen from the figure, six parameters significantly influence the axial stress-strain curve. Consequently, the 13 groups of input parameters,

along with the results of the concrete cylinder strength (f' co) and the corresponding axial strain (εco), are listed in Table 3. To quantify the sensitivity of each parameter, a linear regression analysis is performed. Prior to the regression analysis, the parameters and results are Min-Max normalized to the [0, 1] interval to eliminate the influence of the quantity dimension:

$$X' = \frac{X - X_{min}}{X_{max} - X_{min}} \quad (21)$$

where X is the concerned parameter value of the current model, Xmax and Xmin is the maximum and minimum value for this parameter among all cases, X' is the normalized parameter value.

Table 3. Parametric study on uniaxial compression

Ea (MPa)	Em (MPa)	fc (MPa)	ft (MPa)	ψ (°)	β (°)	f'co (MPa)	εco
45000	20200	56.5	3.7	25	20	41.9	0.00194
55000	20200	56.5	3.7	25	20	39.9	0.00176
65000	20200	56.5	3.7	25	20	38.5	0.00176
55000	15000	56.5	3.7	25	20	36.0	0.00194
55000	25000	56.5	3.7	25	20	42.4	0.00176
55000	20200	46.5	3.7	25	20	35.2	0.00176
55000	20200	66.5	3.7	25	20	44.2	0.00194
55000	20200	56.5	2.7	25	20	35.7	0.00176
55000	20200	56.5	4.7	25	20	42.4	0.00194
55000	20200	56.5	3.7	20	20	38.9	0.00176
55000	20200	56.5	3.7	30	20	41.4	0.00194
55000	20200	56.5	3.7	25	0	38.6	0.00176
55000	20200	56.5	3.7	25	35	40.8	0.00194

The coefficients of f' co and εco are presented in Fig. 7. As can be seen from Fig. 7a, fc, ft, and Em have a significant positive correlation with f' co, while Ea shows a negative correlation with f' co. Since the FE models are loaded in a displacement-controlled manner and the results are output at fixed intervals, εco has only two values. Consequently, Fig. 7b only offers qualitative results indicating that Ea and Em are negatively correlated with εco, whereas the remaining parameters are positively correlated with εco.

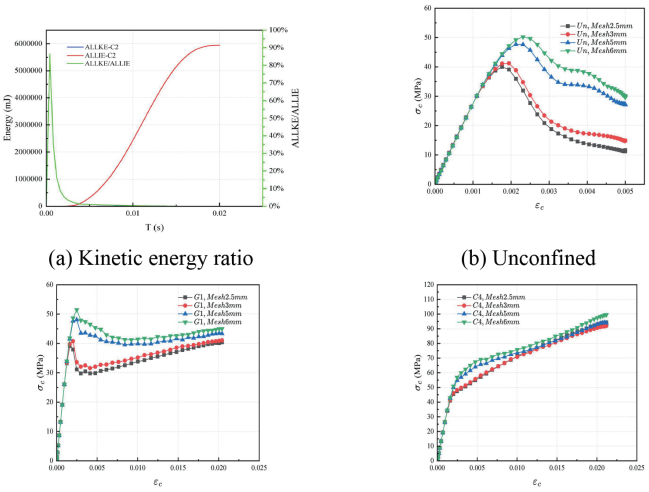

Figure 6. Influence of key parameters on uniaxial compression

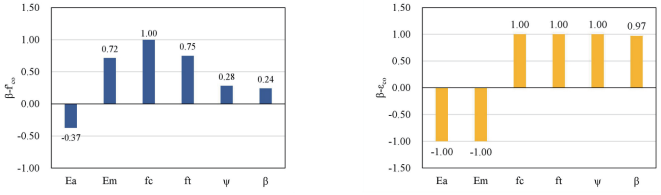

Figure 7. Sensitivity of parameters on uniaxial compression

The parametric study reveals that the uniaxial stress-strain behaviour of the concrete cylinder is significantly influenced by the properties of the mortar matrix, while the influence of the ITZ is relatively less pronounced. To delve deeper into the relationship between the mortar properties and the uniaxial behaviour of the concrete cylinder, a trial-and-error analysis is carried out. By varying fc and Em, the stress-strain curve of the concrete cylinder is optimized to best fit the predictions of the Chinese code [71]. The best-fit values of fc and Em are presented in Table 4. These values can achieve a good agreement with the uniaxial stress-strain curves specified in the Chinese code, as illustrated in Fig. 8 for concrete with f' co ranging from 20 MPa to 60 MPa.

Table 4. Parameters for concrete under uniaxial compression

f'co (MPa)	20	30	40	50	60
fc (MPa)	16	30	45	60	73
Em (MPa)	18290	25907	31730	36638	40413

In summary, the elastic modulus (Em), compressive strength (fc), and tensile strength (ft) are the main influencing factors on the uniaxial stress-strain behaviour of concrete. These three parameters are not independent. Design codes often provide equations for calculating Em and ft based on fc. Additionally, the shape of the axial stress-strain curve of

concrete is determined by that of the mortar. Therefore, the readers may use any axial stress-strain models to model the mortar. The f' co of concrete can be ensured by choosing the Em and fc values in Table 4.

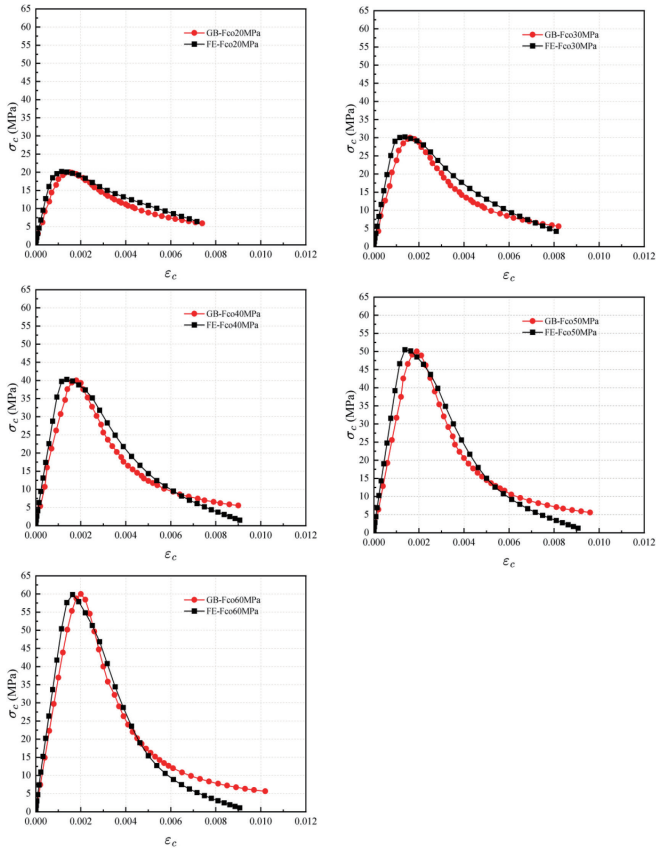

Figure 8. Stress-strain curves for uniaxial compression

3.3.2 FRP-confined concrete

As depicted in Fig. 5c and 5d, the meso-scale model demonstrates second-portion ascending behaviour when confined by FRP, thereby validating the effectiveness of the modelling approach. To determine the remaining parameters, the mortar properties for f' co = 40 MPa in Table 4 are employed, and the other parameters are set to the benchmark values in Table 2. In the model, the concrete is confined by 1-ply GFRP (G1), 2-ply CFRP (C2), and 6-ply CFRP (C6), representing weak, moderate, and heavy confinement, respectively. The results of Jiang and Teng' s [8] analysis-oriented model are presented in Fig.9 as a control, and are denoted by hollow symbols in the figure. This figure shows that with the default parameters values, the meso-scale FE model is in agreement with the analysis-oriented model under weak and moderate confinement. When under heavy confinement, the meso-scale FE model overestimates the axial stress of the FRP-confined concrete in the second ascending stage. Consequently, the next step of the parametric study is to identify the parameters that solely govern the second portion of the stress-strain curve.

The stress-strain curves for the parametric study are presented in Fig. 10. These figures demonstrate that the parameters Em, ψ, β, kS, and GS influence the behaviour of the second portion, whereas the influence of the other parameters is negligible. Since Em has been determined in the first step when determining f' co, there are four parameters to be examined. The axial stress at εc = 0.02 (σc,0.02) is herein employed to quantify the behaviour of the second portion. The four parameters (ψ, β, kS, and GS) and σc,0.02 are summarized in Table 5, with a total of 9 groups of results. Similar to Section 3.3.1, a linear regression analysis is performed on the Min-max normalized parameters, and the coefficients for weakly confined (G1) and heavily confined (C6) concrete are depicted in Fig. 11. The results indicate that the friction angle (β) has the most significant impact on the second portion of the stress-strain curves. The dilation angle (ψ) is more sensitive under heavy confinement, while the shear stiffness (kS) and the fracture energy (GS) are more sensitive under weak confinement. Therefore, from the perspective of the trial-and-error method, the most effective approach is to modify ψ and β under heavy confinement.

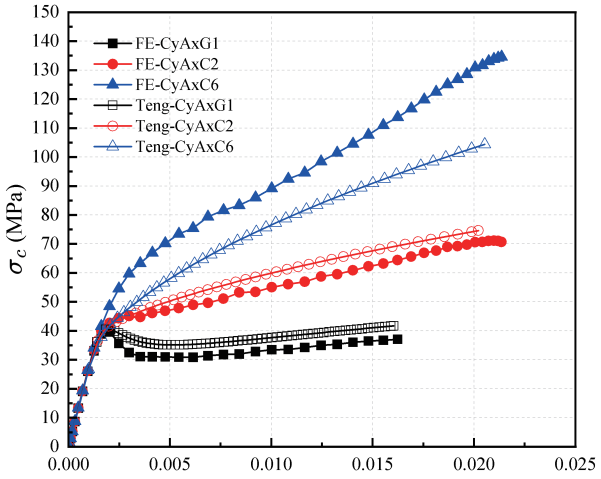

Figure 9. Stress-strain curves for FRP confined concrete using benchmark values

Table 5. Parametric study on FRP confinement

ψ(°)	β(°)	kS(MPa/mm)	GS(N/mm)	σc,0.02-G1(MPa)	σc,0.02-C6(MPa)
20	20	25000	0.75	37.5	123.5
25	20	25000	0.75	39.3	130.5
30	20	25000	0.75	40.6	139.2
25	0	25000	0.75	30.1	106.6
25	35	25000	0.75	43.1	140.8
25	20	15000	0.75	37.3	128.6
25	20	35000	0.75	41.3	133.5
25	20	25000	0.50	35.8	127.8
25	20	25000	1.00	42.0	133.8

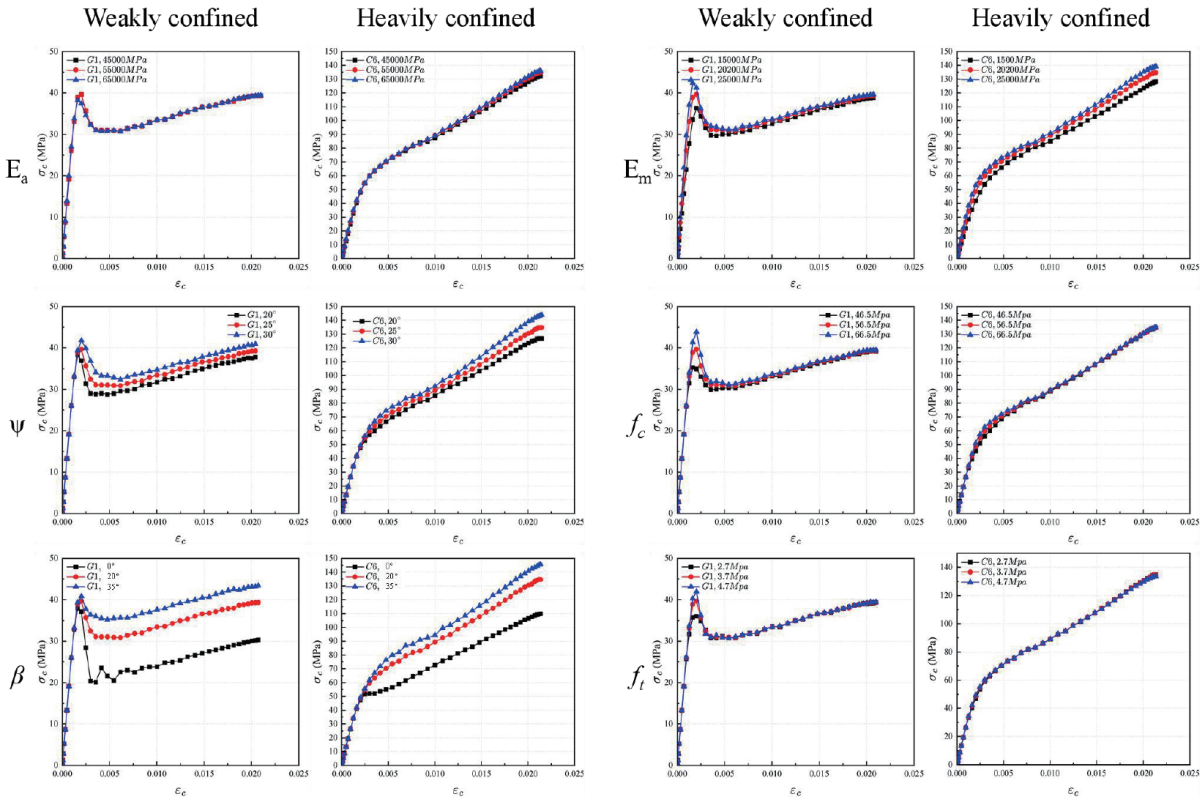

(a) CDP parameters

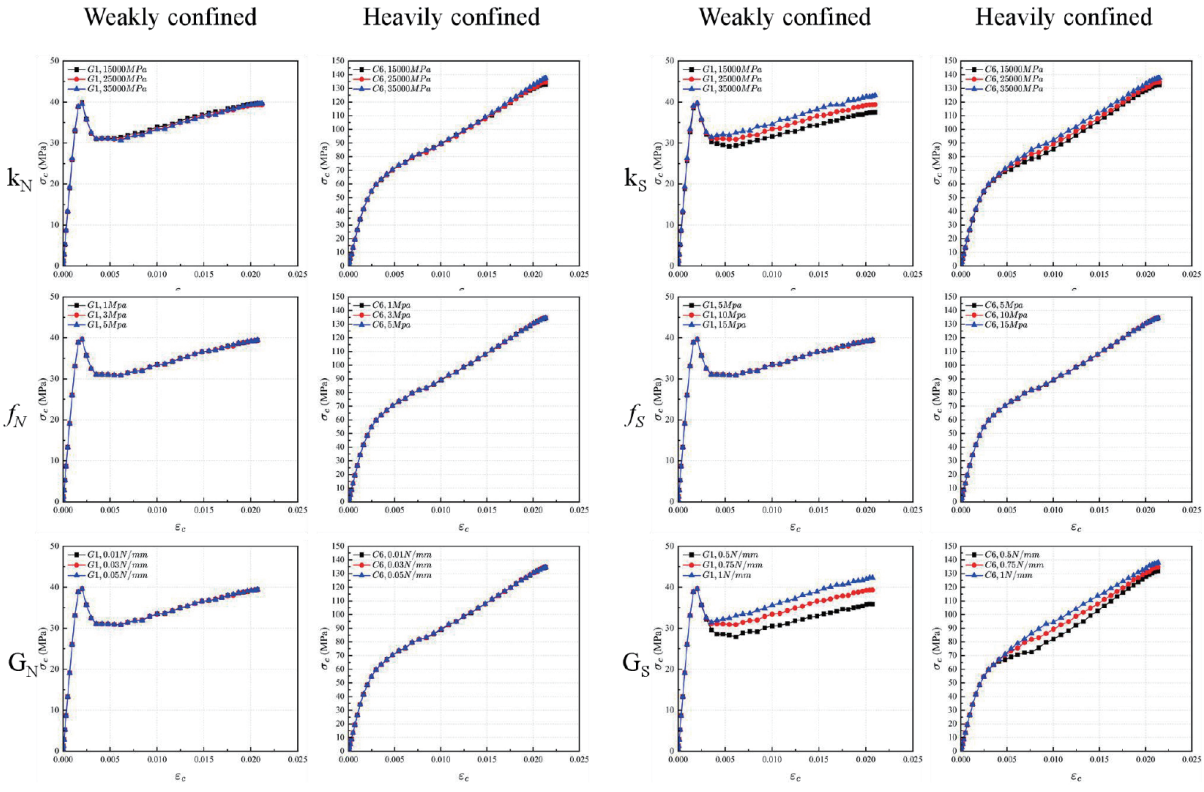

(b) ITZ parameters

Figure 10. Parametric study on FRP confinement

Following this concept, ψ and β are adjusted to enable the concrete under three confinement levels to best fit Jiang and Teng's [8] analysis-oriented model. The results are presented in Fig. 12. The optimal fitting values of (ψ, β) are (35°, 45.5°),(30°, 38.4°), and (5°, 9.1°) for G1, C2, and C6, respectively. Evidently, ψ and β vary with the confining stiffness. However, the variation of these parameters should be related to the internal state of the material rather than the external loading conditions. Therefore, the authors propose that ψ and β change in relation to the second stress invariant J2, as presented in Table 6. For any given J2 value, ψ and β can be interpolated from the table. This can be achieved using the user-subroutine VUSDFLD in ABAQUS [72].

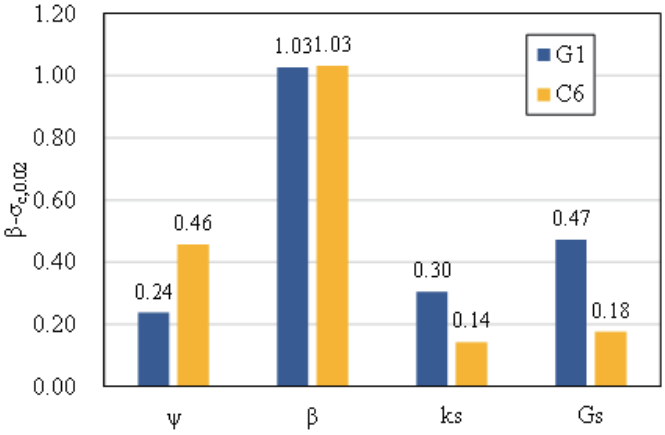

Figure 11. Sensitivity of parameters on FRP confinement

Table 6. Values for ψ and β

J2 (MPa^2)	⩽ 433	=546	⩾ 655
ψ (°)	35	30	5
β (°)	45.5	38.4	9.1

3.4 Proposed parameters

In summary, the determination of the meso-scale model parameters is as follows: (1) Given a known f'co, determine Em and fc using Table 4. If ft is not available, it can be calculated using EQ.19; (2) Input the uniaxial stress-strain curves of the mortar matrix using EQs. 8 - 18; (3) Set ψ and β as field-dependent variables in the CDP model according to Table 6, and define the value of J2 as the field variable using the VUSDFLD subroutine; (4) The remaining parameters can be taken from the benchmark values listed in Table 2. By following these steps, concrete with f'co = 40 MPa confined by different layers of FRP is analysed. The stress-strain curves are presented in Fig. 13, which are in good agreement with Jiang and Teng's [8] analysis-oriented model. Together with the uniaxial curves in Fig. 8, the proposed parameter values are thus verified.

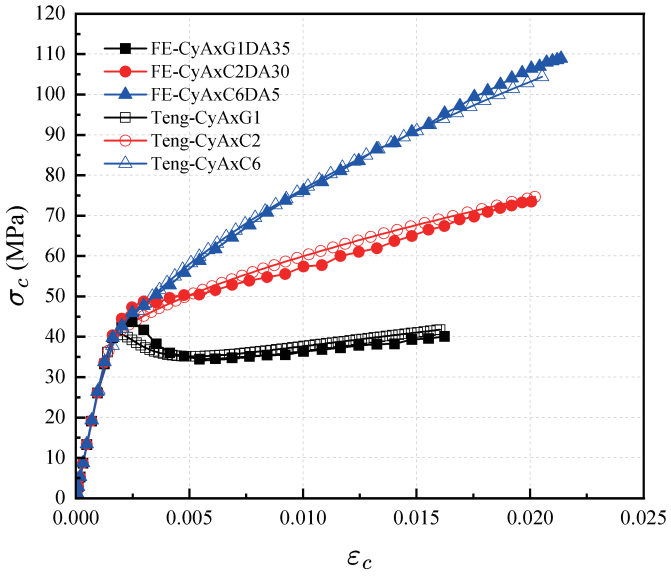

Figure 12. Best-fit stress-strain curves for FRP confined concrete

4. Application of the proposed model on FRP-confined concrete

4.1 Cylinders under concentrated load

The crack patterns of unconfined, 1-ply GFRP-confined (G1), 2-ply CFRP-confined (C2), and 6-ply CFRP-confined (C6) concrete cylinders with a compressive strength of f'co = 40 MPa are depicted in Fig. 14. These patterns are represented by the equivalent tensile plastic strain (PEEQT) contour. The maximum value of the PEEQT is set at 0.025; values beyond this will be presented in grey. For each cylinder, vertical and horizontal slices through the centre at different stress or strain levels are presented. Specifically, for the unconfined cylinder, the contours are presented at the peak strength (σc=f'co) and the ultimate state (εc=0.005). The cracks on the cylinder surface are also shown in Fig. 14a.

At the peak strength, cracks initiate from several large aggregates, and inclined major cracks emerge on the surface. When the ultimate state is reached, the internal cracks propagate vertically, and the surface crack pattern aligns with the observations from standard tests. For the FRP-confined cylinders, the results are presented at the transition point (σc=f'co), the engineering ultimate state (EUS, when εc=0.01) [73], and the ultimate state (εc=0.02). At the transition point, the crack patterns of the three cylinders resemble those of the unconfined concrete. As the confining stiffness increases, the cracked region becomes smaller. For the weakly- and moderately-confined cylinders (G1 and C2), the internal crack patterns are X-shaped, resulting in two uncracked cones at both ends, which is consistent with typical test observations. For the heavily confined cylinder (C6), the internal cracks propagate horizontally. This can be verified by the x-CT results presented in Feng et al. [74].

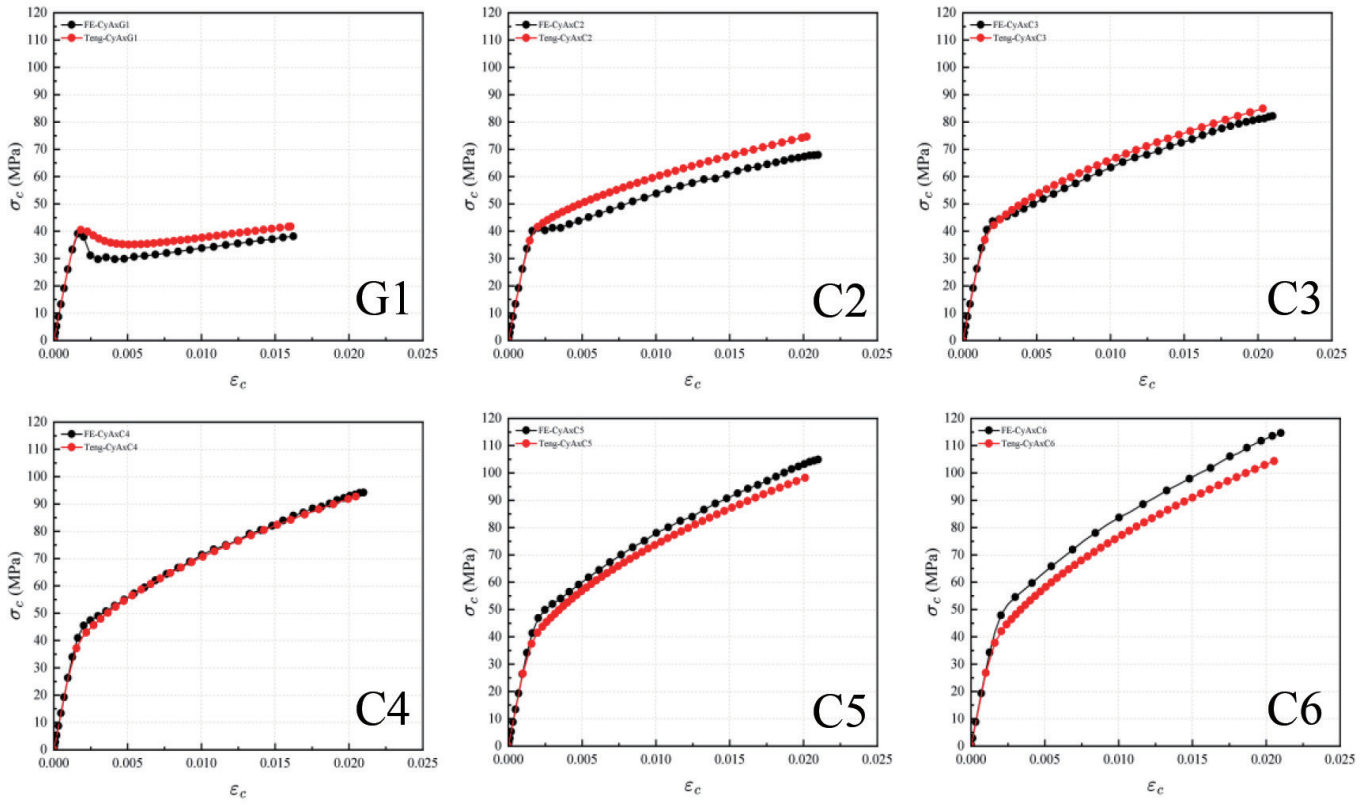

Figure 13. Model verification

4.2 Cylinders under eccentric load

Wu and Jiang [75] carried out an experimental investigation of FRP-confined concrete cylinders under eccentric compression. The concrete cylinders had a diameter of 150 mm and a height of 300 mm. These cylinders were confined by 2-ply CFRP, which had a tensile modulus of 230 GPa and a nominal thickness of 0.167 mm/ply. The strength of the unconfined concrete was 30.1 MPa. Five different eccentricities, namely 10 mm, 20 mm, 30 mm, 40 mm, and 50 mm, were examined. Following the proposed method, the tests conducted by Wu and Jiang [75] were modelled.

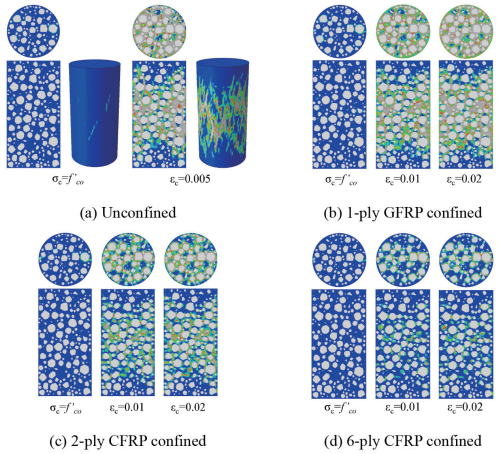

Figure 14. Crack patterns of concrete cylinders under axial compression

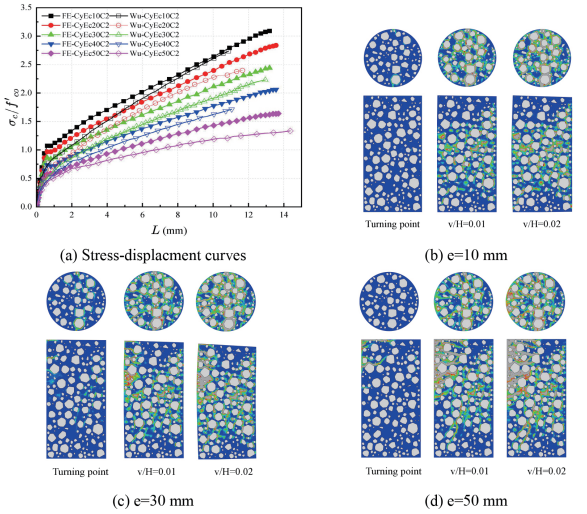

Figure 15. FRP confined cylinders subjected to eccentric load

4.3 Prisms under concentrated load

The efficiency of FRP confinements for concrete with rectangular sections is significantly lower than that for cylinders due to the non-uniform stress distribution. Using the currently proposed meso-scale finite element (FE) model, the stress distribution of FRP-confined concrete prisms with different corner radii is investigated. The tests carried out by Wang and Wu [76] are simulated. In the test, the prism had a

cross-sectional dimension of 150 mm × 150 mm and a height of 300 mm. The unconfined concrete strength was 31.7 MPa, and the prisms were confined by two-ply CFRP with a tensile modulus of 230.5 GPa and a nominal thickness of 0.165 mm per ply.

The axial stress-strain curves of both the test results and the model predictions are plotted in Fig. 16. The simulated curves match the test results well, thus validating the proposed model. Corner radii of 15 mm, 30 mm, and 45 mm were selected in the current model for demonstration. To examine the axial stress distribution, the mid-height cross-section of the prism is evenly divided into a 7×7 grid, as shown in Fig. 17. The resultant section force Fg is obtained from each grid, and the average compression strain is calculated as σc,g = Fg/Ag, where Ag is the actual grid area. The stress distributions of the three models are presented in Fig. 17. Four stress levels with average section stresses of 0.8f' co, 1.0 f' co, 1.2 f' co, and 1.4 f' co are shown for each model. In the figure, the average sectional stress is represented by a grey translucent plane.

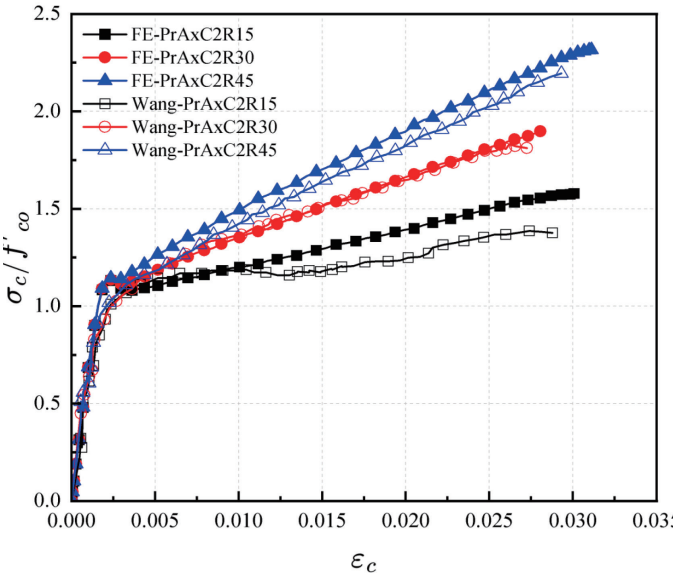

Figure 16. Stress-strain curves for concrete prisms under axial compression

As can be seen from Fig. 18, prior to the transition point (0.8 f' co), the axial stress shows a uniform distribution, excluding the heterogeneity of the meso-scale model. At the transition point (1.0 f' co), the stress in the core of the square section becomes higher than that on the four sides. After the transition point (1.2 f' co and 1.4 f' co), for the R = 15 mm prism, the stress in the core and at the four corners is higher than the average value, and the stress in the core is higher than that at the corners. The stress distribution of the R = 30 mm prism is similar to that of the R = 15 mm prism, but the difference in stress between the core and the four corners is smaller. For the R = 45 mm prism, the stress is concentrated only at the core. The stress on all four sides and at the corners is below the average. Therefore, when developing an analytical model for FRP confinement based on the effectively confined region theory [6], the influence of the corner radius on the shape of the effectively confined region should be taken into account.

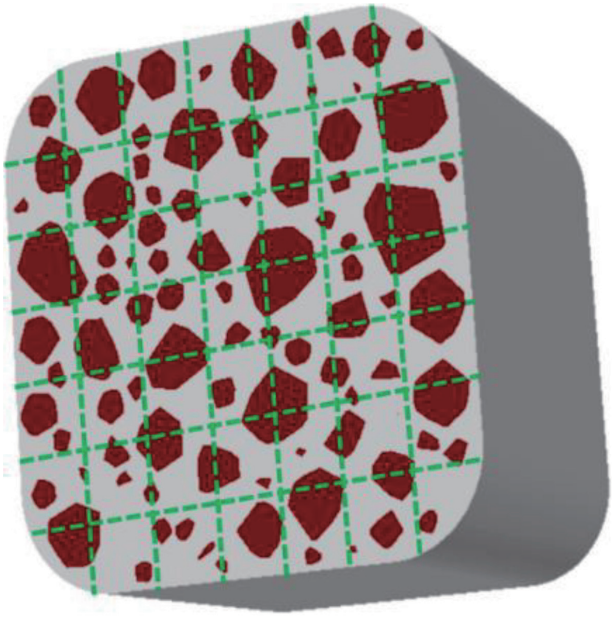

Figure 17. Gridding of the cross section

4.4 Prisms under eccentric load

The prism models constructed in the previous section, with a corner radius of R=30 mm, are eccentrically loaded to examine the stress distribution of FRP-confined concrete prisms under eccentric compression. Eccentricities of e=12.5 mm and e=25 mm are selected for demonstration purposes. The stress-strain curves of the models are presented in Fig. 19. The stress distributions of the two models are extracted in the same manner and plotted in Fig. 20.

Some studies assume a linear distribution of the compression stress. However, as can be observed from Fig. 20, this assumption is only valid prior to the transition point (0.8 f' co). When the stress-strain curve enters the second stage, the stress begins to concentrate in the core and at the two corners in the bending direction. With a further increase in the average stress level, the stress at the two compressed corners becomes significantly higher than the average, while the core stress also exceeds the average. To more clearly illustrate this phenomenon, the stress along two key paths is extracted from the model with e=25 mm at 1.4 f' co and plotted in Fig. 21. The two paths are y=0 and x=62.5, as schematically shown in Fig. 21a. As depicted in Fig. 21b, along the y=0 path, the compression stress remains at a relatively high value within the core region and decreases at the compression edge, thus deviating from the linear distribution assumption. As shown in Fig. 21c, at the edge of x = 62.5, the compressive stress is concentrated in the two corners, approximately twice as high as that in the middle of the edge. Based on the results, for an FRP-confined square-section concrete column under eccentric load, the compressive stress is concentrated at the core and the compressed corners of the square section. Thus, it indicates that applying additional localized confinement in these areas is highly effective in enhancing the performance of concrete columns [17][18][19].

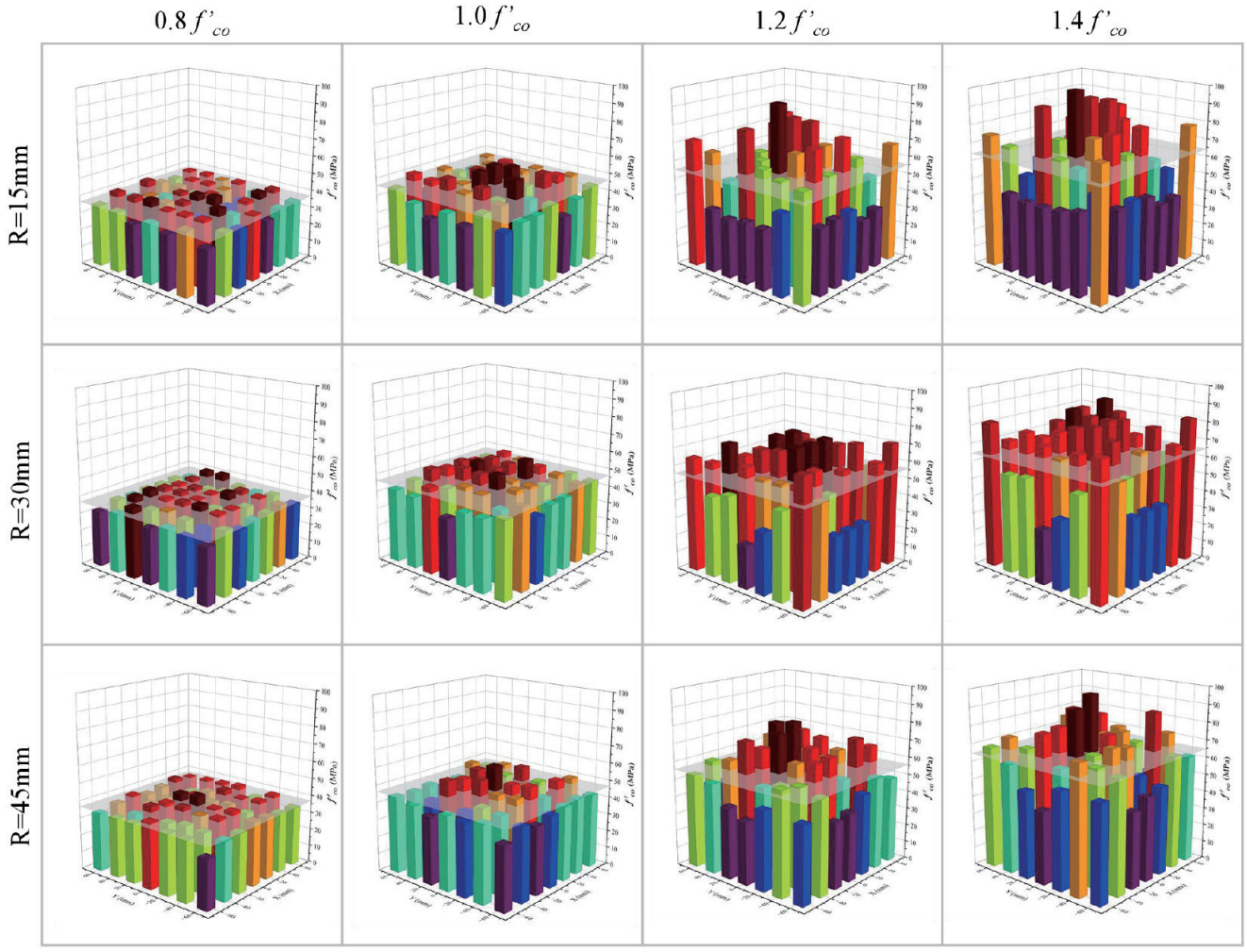

Figure 18. Stress distribution of concrete prisms under axial compression

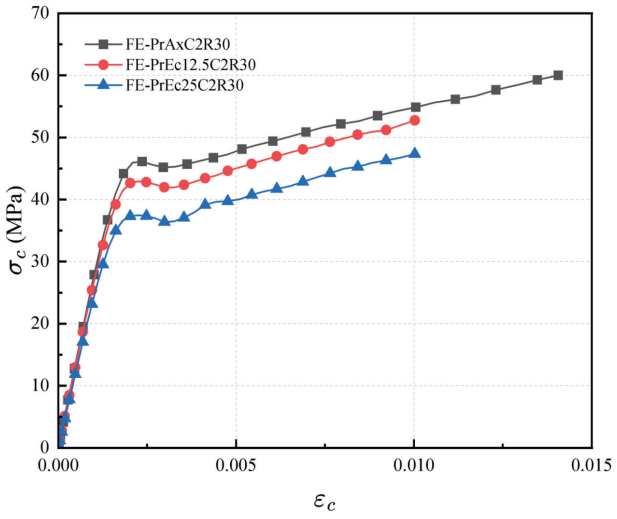

Figure 19. Stress-strain curves for concrete prisms under eccentric compression

5. Conclusions

In this research, a systematic modelling approach and the values of key parameters for meso-scale finite element models of FRP-confined concrete are proposed. Using the proposed model, simulations are carried out on FRP-confined concrete cylinders and prisms under axial and eccentric compression. The results show the internal damage pattern and the actual stress distribution within the concrete, uncovering the physical mechanism of passive confinement. The following conclusions can be reached:

(1) Under the current modelling strategy, the macro-scale behaviour of unconfined concrete is highly reliant on the uniaxial behaviour of the mortar matrix. According to the proposed approach, the uniaxial compression of concrete can be accurately modelled.

(2) The second-stage behaviour of FRP-confined concrete is primarily governed by the tri-axial constitutive model of the mortar matrix. The friction angle and dilation angle of the mortar vary with the stress state of the mortar rather than being constant values.

(3) An X-shaped cracking zone can be detected within axially compressed FRP-confined concrete cylinders. As the confining stiffness increases, the angles of the crack patterns relative to the horizontal become smaller. In the case of heavily confined concrete, the internal cracks propagate horizontally.

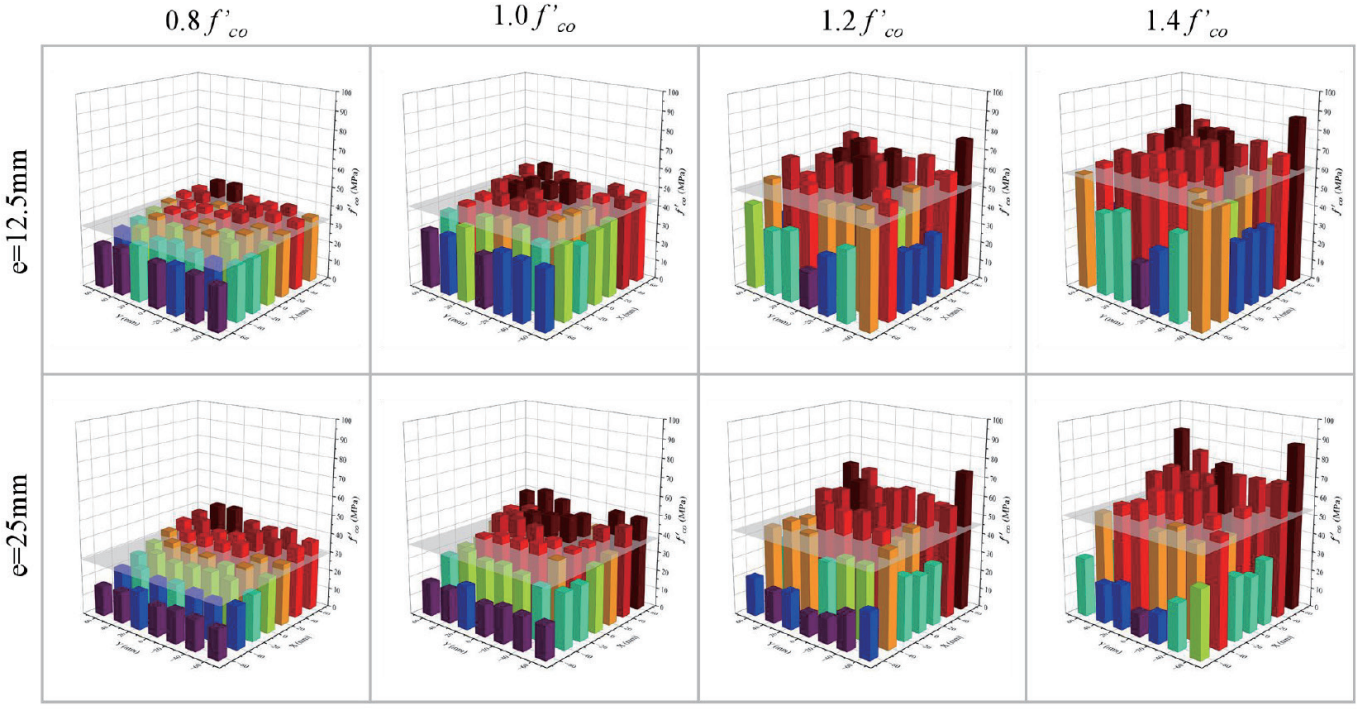

Figure 20. Stress distribution of concrete prisms under eccentric compression

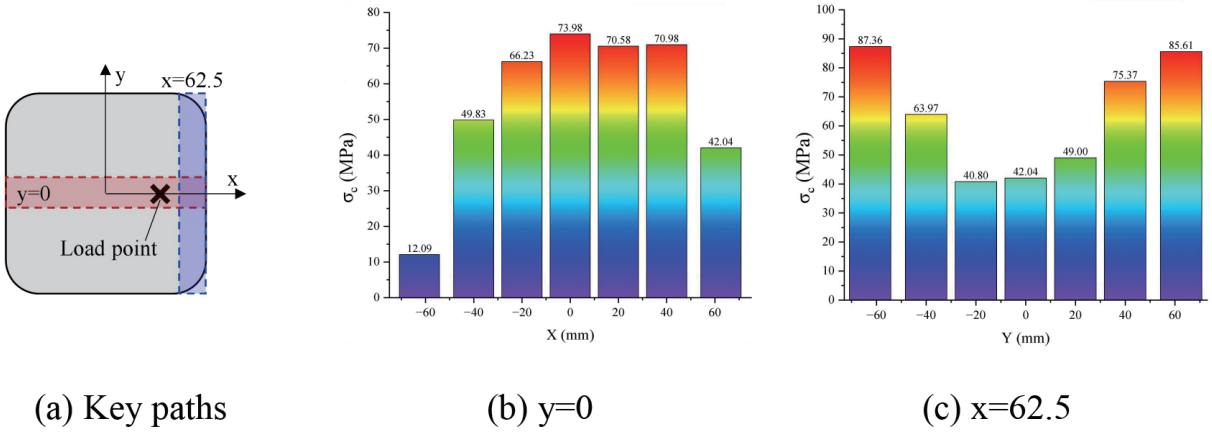

Figure 21. Stress distribution on key paths for e=25mm

(4) In FRP-confined concrete prisms, the compression stress is concentrated in the core region and the corners. When subjected to axial compression, an increase in the corner radii alleviates the stress at the four corners. When the prism is under an eccentric load, the stress distribution does not conform to the linear distribution assumption; specifically, the stress in the middle of the compressed edge is significantly lower than that in the corners and the core region.

Declaration of competing interest

No.

Acknowledgement

This work is supported by the National Natural Science Foundation of China (No. 52378207, 52208251 and U22A20244).

Notation list

Ag	Grid area
dij	The distance between Oi and Oj
diB	The distance between Oi and boundary
D	Damage variable of ITZ
e	Eccentricity

Ea	Elastic modulus of aggregates
Em	Elastic modulus of mortar matrix
f’ co	Compressive strength of concrete cylinder
fb	Biaxial compressive strength of mortar matrix
fc	Compressive strength of mortar matrix
ft	Tensile strength of mortar matrix
fN	Normal strength of ITZ
fS	Shear strength of ITZ
Fg	Resultant force of a grid
GN	Mode I fracture energy of ITZ
GS	Mode II fracture energy of ITZ
J2	Second stress invariant
kN	Normal stiffness of ITZ
kS	Shear stiffness of ITZ
Oi	The reference point of the ith aggregate
p	Effective hydraulic pressure
q	Effective Mises equivalent stress
R	Corner radius
ri	The radius of the ith aggregate
x, y	Coordinates for square concrete section
xi, yi, zi	Coordinate of the ith aggregate
xik, yik, zik	The coordinate of the kth vertices in the ith aggregate
β	Friction angle of mortar matrix
δN	Normal displacement of ITZ
δS	Shear displacement of ITZ
εc,r	Compression strain of mortar matrix corresponding to fc
εt,r	Tensile strain of mortar matrix corresponding to ft
εco	Compressive strain corresponding to f’ co
εc	Compressive strain of concrete cylinder
νa	Poisson’ s ratio of aggregates
νm	Poisson’ s ratio of mortar matrix
σN	Normal stress of ITZ
σc	Compressive stress of mortar matrix
σt	Tensile stress of mortar matrix
σc,0.02	Compressive stress of concrete corresponding to εc=0.02
σc,g	Nominal average stress of a grid
σmax	Effective maximum principal stress
σcεcpl	Effective compressive cohesion stress
τ	Shear stress of ITZ
ψ	Dilation angle of mortar matrix

References

[1] Teng JG, Chen JF, Smith ST, Lam L. FRP-Strengthened RC Structures. London, UK: Weily; 2002.

[2] Richart FE, Brandtzaeg A, Brown RL. A study of the failure of concrete under combined compressive stresses. Bulletin No.185, Engineering Experiment Station, University of Illinois, Urbana, Illinois; 1928.

[3] Richart FE, Brandtzaeg A, Brown RL. The failure of plain and spirally reinforced concrete in compression. Bulletin No.190, Engineering Experiment Station, University of Illinois, Urbana, Illinois; 1928.

[4] Sfer D, Carol I, Gettu R, Etse G. Study of the behavior of concrete under triaxial compression. Journal of engineering mechanics. 2002; 128(2): 156-163.

[5] Candappa DC, Sanjayan JG, Setunge S. Complete triaxial stress-strain curves of high-strength concrete. Journal of materials in civil engineering. 2001; 13(3): 209-215.

[6] Mander JB, Priestley MJ, Park R. Theoretical stress-strain model for confined concrete. Journal of structural engineering. 1988; 114(8): 1804-1826.

[7] Lam L, Teng JG. Design-oriented stress–strain model for FRP-confined concrete. Construction and building materials. 2003;17(6-7):471-489.

[8] Jiang T, Teng JG. Analysis-oriented stress–strain models for FRP–confined concrete. Engineering Structures. 2007;29(11):2968-2986.

[9] Teng JG, Lam L. Behaviour and modelling of fibre reinforced polymer-confined concrete. Journal of structural engineering. 2004;130(11):1713-1723.

[10] Lam L, Teng JG. Ultimate condition of fibre reinforced polymer-confined concrete. Journal of Composites for Construction. 2004;8(6):539-548.

[11] Ahmed A. A Review on the Effectiveness of FRP and Hybrid Wrappings for Strengthening Concrete Columns. Results in Engineering. 2025:106023.

[12] Fardis MN, Khalili HH. FRP-encased concrete as a structural material. Magazine of concrete research. 1982;34(121):191-202.

[13] Mirmiran A, Shahawy M. Behaviour of concrete columns confined by fibre composites. Journal of structural engineering. 1997;123(5):583-590.

[14] Fam AZ, Rizkalla SH. Behaviour of axially loaded concrete-filled circular fiber-reinforced polymer tubes. Structural Journal. 2001;98(3):280-289.

[15] Yu T, Teng JG, Wong YL. Stress-strain behaviour of concrete in hybrid FRP-concrete-steel double-skin tubular columns. Journal of structural engineering. 2010; 136(4): 379-389.

[16] Yu T, Zhang B, Cao YB, Teng JG. Behaviour of hybrid FRP-concrete-steel double-skin tubular columns subjected to cyclic axial compression. Thin-walled structures. 2012; 61: 196-203.

[17] Wang Z, Feng P, Zhao Y, Yu T. FRP-confined concrete core-encased rebar for RC columns: Concept and axial compressive behaviour. Composite Structures. 2019; 222: 110915.
[18] Hu L, Feng P, Lin H, Yang JQ, Qiang H. Seismic performance of composite shear walls with embedded FCCCs in boundary elements. Composite Structures. 2021; 257: 113126.
[19] Hu L, Feng P, Yang JQ, Li Z. Shear behaviour of FRP-confined concrete/UHPC core-encased rebar: Experimental investigation and design method. Engineering Structures. 2023 Jun 1; 284: 115951.
[20] Ozbakkaloglu T, Lim JC, Vincent T. FRP-confined concrete in circular sections: Review and assessment of stress–strain models. Engineering Structures. 2013; 49: 1068-1088.
[21] Teng JG, Jiang T, Lam L, Luo YZ. Refinement of a design-oriented stress–strain model for FRP-confined concrete. Journal of composites for construction. 2009; 13(4): 269-278.
[22] Mirmiran A, Shahawy M. Dilation characteristics of confined concrete. Mechanics of Cohesive‐frictional Materials: An International Journal on Experiments, Modelling and Computation of Materials and Structures. 1997; 2(3): 237-249.
[23] Teng JG, Huang YL, Lam L, Ye LP. Theoretical model for fiber-reinforced polymer-confined concrete. Journal of composites for construction. 2007; 11(2): 201-210.
[24] Kwan AK, Dong CX, Ho JC. Axial and lateral stress–strain model for FRP confined concrete. Engineering Structures. 2015; 99: 285-295.
[25] Yang JQ, Feng P. Analysis-oriented models for FRP-confined concrete: 3D interpretation and general methodology. Engineering Structures. 2020; 216: 110749.
[26] Yang JQ, Feng P. Analysis-oriented model for FRP confined high-strength concrete: 3D interpretation of path dependency. Composite Structures. 2021; 278: 114695.
[27] Li Z, Feng P, Yang JQ. Analysis-oriented model for FRP tube-confined concrete: 3D interpretation of biaxial tube behaviour. Engineering Structures. 2022; 272: 114987.
[28] Yang JQ, Li X, Li Z, Feng P, Wu L. Influence of fibre undulation on the biaxial behaviour of filament-wound FRP tubes in concrete-filled FRP tubes. Composite Structures. 2025:119388.
[29] Bousias SN, Triantafillou TC, Fardis MN, Spathis L, O' Regan BA. Fiber-reinforced polymer retrofitting of rectangular reinforced concrete columns with or without corrosion. Structural Journal. 2004; 101(4): 512-520.
[30] Wang Z, Li Z, Yang JQ, Huang F, Feng P. Axial compressive and seismic performance of GFRP wrapped square RC columns with different scales. Journal of Building Engineering. 2022; 62: 105342.
[31] Dang Z, Feng P, Suong S, Tang L. Quasi-static cyclic tests of FRP-confined steel-reinforced HPFRCC circular columns. Engineering Structures. 2024; 318: 118745.
[32] Hou S, Zhang HB, Ou JP. A PZT-based smart aggregate for compressive seismic stress monitoring. Smart Materials and Structures. 2012; 21(10): 105035.
[33] Hou S, Zhang HB, Ou JP. A PZT-based smart aggregate for seismic shear stress monitoring. Smart materials and Structures. 2013; 22(6): 065012.
[34] Pan HH, Guan JC. Stress and strain behaviour monitoring of concrete through electromechanical impedance using piezoelectric cement sensor and PZT sensor. Construction and Building Materials. 2022; 324: 126685.
[35] Li PD, Wu YF. Damage evolution and full-field 3D strain distribution in passively confined concrete. Cement and Concrete Composites. 2023; 138: 104979.
[36] Zeng Y, Xu L, Yu M, Tong D, Gao B, Huang L, Chi Y. Stability of slender GFRP tube-confined UHPC-filled steel-encased column under axial compression: Experiment and mesoscale modelling. Thin-Walled Structures. 2024; 205: 112564.
[37] Yu T, Teng JG, Wong YL, Dong SL. Finite element modelling of confined concrete-I: Drucker–Prager type plasticity model. Engineering structures. 2010; 32(3): 665-679.
[38] Yu T, Teng JG, Wong YL, Dong SL. Finite element modelling of confined concrete-II: Plastic-damage model. Engineering structures. 2010; 32(3): 680-691.
[39] Zheng BT, Teng JG. A plasticity constitutive model for concrete under multiaxial compression. Engineering Structures. 2022; 251: 113435.
[40] Lin G, Teng JG. Stress-strain model for FRP-confined concrete in eccentrically loaded circular columns. Journal of Composites for Construction. 2019 Jun 1;23(3):04019017.
[41] Lin G, Teng JG. Advanced stress-strain model for FRP-confined concrete in square columns. Composites Part B: Engineering. 2020; 197: 108149.
[42] Teng JG, Wu JY, Casalboni S, Xiao QG, Zhao Y. Behaviour and modelling of fibre-reinforced polymer-confined concrete in elliptical columns. Advances in Structural Engineering. 2016; 19(9): 1359-1378.
[43] Zheng Z, Tian C, Wei X, Zeng C. Numerical investigation and ANN-based prediction on compressive strength and size effect using the concrete mesoscale concretization model. Case Studies in Construction Materials. 2022; 16: e01056.
[44] Huang Y, Yang Z, Ren W, Liu G, Zhang C. 3D meso-scale fracture modelling and validation of concrete based on in-situ X-ray Computed Tomography images using damage plasticity model. International Journal of Solids and Structures. 2015; 7: 40-52.
[45] Chen B, Yu H, Zhang J, Ma H, Tian F. Effects of the embedding of cohesive zone model on the mesoscopic fracture behaviour of Concrete: A case study of uniaxial tension and compression tests. Engineering failure analysis. 2022;142:106709.
[46] Xie C, Chen X, Yang JQ, Bao C, Feng P. Mesoscale simulation method for preplaced aggregate concrete based on physics engine. Case Studies in Construction Materials. 2024;21:e03687.
[47] Jin L, Yu W, Su X, Zhang S, Du X, Han J, Li D. Effect of cross-section size on the flexural failure behavior of RC cantilever beams under low cyclic and monotonic lateral loadings. Engineering Structures. 2018;156:567-86.
[48] Jin L, Yu W, Du X, Yang W. Mesoscopic numerical simulation of dynamic size effect on the splitting-tensile strength of concrete. Engineering Fracture Mechanics. 2019;209:317-32.
[49] Jin L, Li J, Yu W, Du X. Mesoscopic simulations on the strength and size effect of concrete under biaxial loading. Engineering Fracture Mechanics. 2021; 53: 07870.
[50] Liu T, Qin S, Zou D, Song W, Teng J. Mesoscopic modelling method of concrete based on statistical analysis of CT images. Construction and Building Materials. 2018;192:429-41.
[51] Xu Y, Chen S. A method for modelling the damage behaviour of concrete with a three-phase mesostructure. Construction and Building Materials. 2016 Jan 15;102:26-38.
[52] Chen H, Xu B, Mo YL, Zhou T. Behavior of meso-scale heterogeneous concrete under uniaxial tensile and compressive loadings. Construction and Building Materials. 2018;178:418-31.

[53] Zhou Y, Jin H, Wang B. Modeling and mechanical influence of meso-scale concrete considering actual aggregate shapes. Construction and Building Materials. 2019; 28: 16785.
[54] Zhang Y, Chen Q, Wang Z, Zhang J, Wang Z, Li Z. 3D mesoscale fracture analysis of concrete under complex loading. Engineering Fracture Mechanics. 2019; 20: 106646.
[55] Naderi S, Tu W, Zhang M. Meso-scale modelling of compressive fracture in concrete with irregularly shaped aggregates. Cement and concrete research. 2021; 140: 106317.
[56] Naderi S, Zhang M. Meso-scale modelling of static and dynamic tensile fracture of concrete accounting for real-shape aggregates. Cement and Concrete Composites. 2021;116:103889.
[57] Zhou R, Lu Y. A mesoscale interface approach to modelling fractures in concrete for material investigation. Construction and Building Materials. 2018;165:608-20.
[58] Wang J, Jivkov AP, Li QM, Engelberg DL. Experimental and numerical investigation of mortar and ITZ parameters in meso-scale models of concrete. Theoretical and Applied Fracture Mechanics. 2020;109:102722.
[59] Zhou G, Xu Z. 3D mesoscale investigation on the compressive fracture of concrete with different aggregate shapes and interface transition zones. Construction and Building Materials. 2023;393:132111.
[60] Huang Y, Hu S, Gu Z, Sun Y. Fracture behaviour and energy analysis of 3D concrete mesostructure under uniaxial compression. Materials. 2019;12(12):1929.
[61] Huang YQ, Hu SW, Sun YY. The effect of inner friction on concrete fracture behaviour under biaxial compression: A 3D mesostructure study. Materials. 2019;12(23):3880.
[62] Xiong X, Xiao Q. Meso-scale simulation of concrete based on fracture and interaction behaviour. Applied Sciences. 2019;9(15):2986.
[63] Zhang L, Sun X, Xie H, Feng J. Three-dimensional mesoscale modelling and failure mechanism of concrete with four-phase. Journal of Building Engineering. 2023; 64: 105693.
[64] Zhang L, Sun X, Xie H, Feng J. Three-dimension mesoscale model of concrete by random placement algorithm and its failure mechanism analysis. Engineering Failure Analysis. 2023;152:107486.
[65] Geng J, Liu C. A methodology for parameter identification and calibration of the cohesive element based meso-scale concrete model. Construction and Building Materials. 2023;393:132075.
[66] Ying J, Guo J. Fracture behaviour of real coarse aggregate distributed concrete under uniaxial compressive load based on cohesive zone model. Materials. 2021;14(15):4314.
[67] Wang B, Zhu E, Zhang Z. Microscale fracture damage analysis of lightweight aggregate concrete under tension and compression based on cohesive zone model. Journal of Engineering Mechanics. 2022;148(2):04021153.
[68] Trawiński W, Bobiński J, Tejchman J. Two-dimensional simulations of concrete fracture at aggregate level with cohesive elements based on X-ray μCT images. Engineering Fracture Mechanics. 2016;168:204-26.
[69] Lee J, Fenves GL. Plastic-damage model for cyclic loading of concrete structures. Journal of engineering mechanics. 1998;124(8):892-900.
[70] Benzeggagh ML, Kenane MJ. Measurement of mixed-mode delamination fracture toughness of unidirectional glass/epoxy composites with mixed-mode bending apparatus. Composites science and technology. 1996;56(4):439-49.
[71] China National Standardization Management Committee. Code for Design of Concrete Structures. GB 50010-2010. Beijing: China Architecture & Building Press, 2010.
[72] Dassault Systems. ABAQUS Documentation. Dassault Systems, 2020.
[73] Feng P, Yang JQ, Li Z. Hybrid members incorporating FRP confined concrete core. In Proceedings: 7th Asia-Pacific Conference on FRP in Structures (APFIS 2019), Surfers Paradise, Gold Coast, Australia, 13-10/Dec/2019.
[74] Feng, P., Yang, JQ., Li, Z. FRP Confined Concrete: What, Why, and How?. In: Ilki A, Ispir M, Inci P. (eds) 10th International Conference on FRP Composites in Civil Engineering. CICE 2021. Lecture Notes in Civil Engineering, vol 198. Springer, Cham. 2022.
[75] Wu YF, Jiang C. Effect of load eccentricity on the stress–strain relationship of FRP-confined concrete columns. Composite structures. 2013;98:228-41.
[76] Wang LM, Wu YF. Effect of corner radius on the performance of CFRP-confined square concrete columns: Test. Engineering structures. 2008;30(2):493-505.